



Aeromagnetic and Radiometric Data Interpretation to Delineate the Structural Elements and Probable Precambrian Mineralization Zones: a Case Study, Egypt

Khalid S. Essa¹ · Marc Munsch² · Mohamed A. S. Youssef³ · Ezz El Din Abdel Hakim Khalaf⁴

Received: 18 January 2021 / Accepted: 26 August 2022 / Published online: 22 September 2022
© The Author(s) 2022

Abstract

This study focused on joint interpretation of the aeromagnetic and radiometric data to allocate and describe the structural elements and mineralization zones such as uranium, gold, and sulfide in the Gebel Umm Tineidba and its surroundings, Eastern Desert, Egypt. The study region is covered by exposures of Precambrian rocks such as gneisses, migmatites, ophiolitic mélange, metavolcanics, younger granites, and Quaternary sedimentary covers. The application of the total intensity magnetic and reduced-to-pole maps, power spectrum, analytic signal, tilt-angle, and local wavenumber maps helps in recognizing magnetic sources distribution, lineament features, and mineral zones delineation. The obtained results indicate that the depths of the deeper NE–SW, NNE–SSW, and N–S trending structures extend from 400 to 1750 m and shallower ones range from 100 to 400 m. Finally, the main trends of these structures affect the probable mineralization zones.

Keywords Aeromagnetic data · Gamma-ray data · Mineral exploration · Lineament · Depth

1 Introduction

Generally, aeromagnetic data have been utilized in exploring and recognizing mineralization districts, hydrocarbon exploration, geothermal activity, archaeology site investigations, and engineering applications [1–11].

These data have delivered significant information at various levels of detail, extending from contacts among zones and layering within zones to faults-controlled intrusive dykes that can affect the mine planning [12–15]. Furthermore, the aeromagnetic measurements have the benefit of being able to quickly cover difficult to access areas covering a wide range [16–18]. Recently,

magnetic data interpretation has been done using methods that include simple geologic models and magnetic gradients parameters to recognize the shallower and deeper structures and distinguish the structure features, which control the mineralization zones [19–25].

This article deals mainly with delineation and elucidation of the structures that controlled the mineralization zones utilizing the airborne magnetic and the gamma-ray aero-spectroscopy records in the exposed Neoproterozoic rocks of the Gabel Umm Tineidba and its environs, South Eastern Desert, Egypt (Fig. 1). The whole district is regionally covered by exposures such as gneisses, migmatites, ophiolitic mélange, metavolcanics, younger granites, and Quaternary sedimentary covers. The total magnetic data were processed and elucidated using several techniques such as a reduced-to-pole (RTP), radially average power spectrum (PS), analytical signal (A_s), tilt-angle (T_g), and local wavenumber (LW) to reveal the tectonic and geological structures that are required to locate possible uranium, gold, and sulfide-rich mineralization zones. By using the above-mentioned methods, it permits mapping of the economic mineralized zones and their associated-structures.

✉ Khalid S. Essa
khalid_sa_essa@cu.edu.eg; essa@sci.cu.edu.eg

¹ Geophysics Department, Faculty of Science, Cairo University, P.O. 12613, Giza, Egypt

² Institut de Physique du Globe de Strasbourg, EOST, CNRS, University of Strasbourg, Strasbourg, France

³ Nuclear Materials Authority, P.O. 530, Cairo, Egypt

⁴ Geology Department, Faculty of Science, Cairo University, P.O. 12613, Giza, Egypt

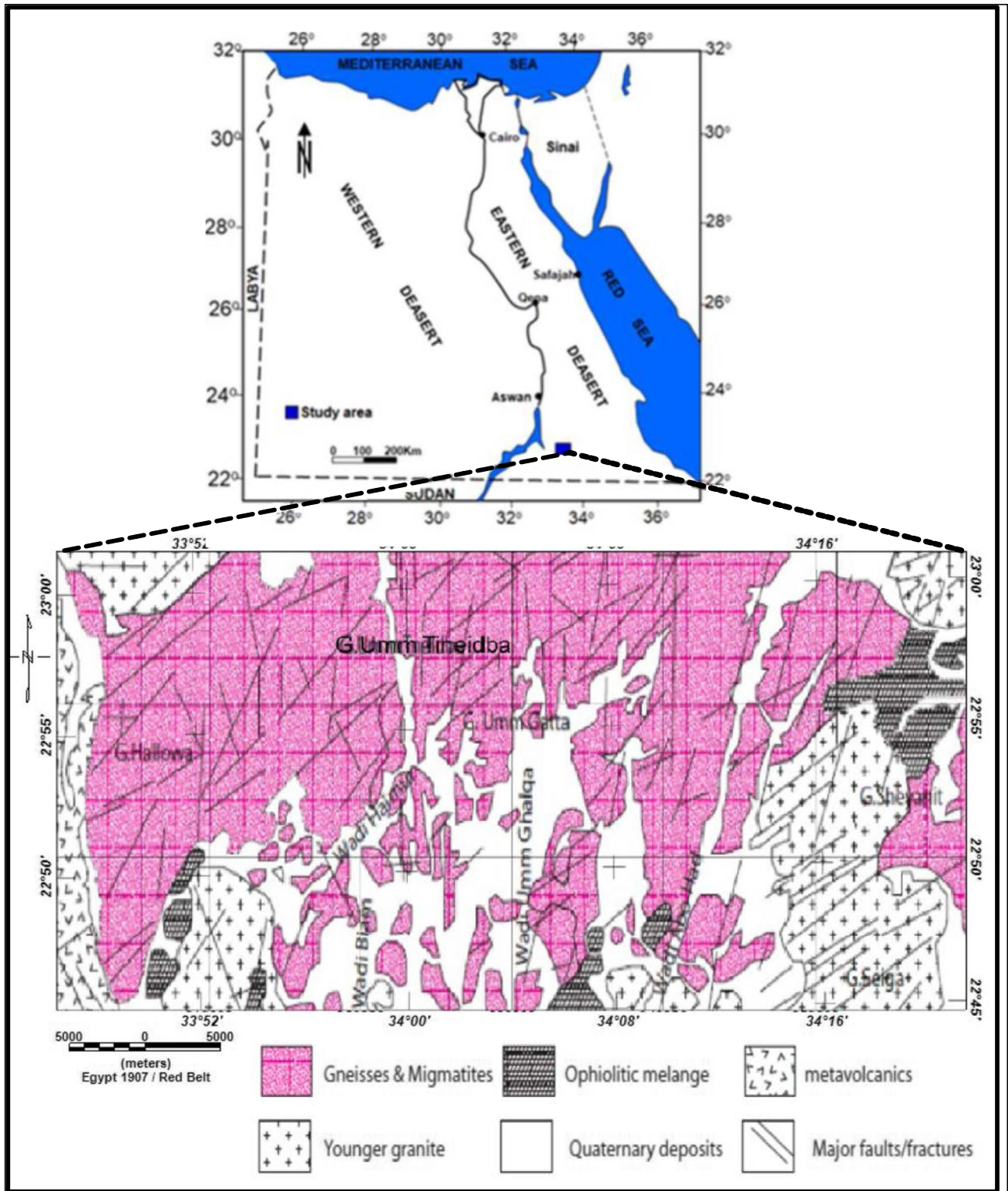


Fig. 1 The location and the geological map of Umm Tineidba area, Southern Eastern Desert, Egypt [30]

2 Geological Backgrounds

The study area is part of the Neoproterozoic Arabian-Nubian Shield (ANS) fluctuating in age from 900 to 550 Ma. The ANS can be characterized by a complex amalgam of arc, ophiolite, and micro-continental terranes that resulted from the Neoproterozoic closure of the Mozambique Ocean [26–30]. Three chief Neoproterozoic rock units involving gneisses and migmatites, dissected ophiolites/ophiolitic mélange, and island arc volcano-sedimentary rocks have been described in South Eastern Desert, Egypt [31, 32]. Younger gabbroic to granitic intrusions invade the three units underlying Quaternary deposits (Fig. 1).

2.1 Gneisses and Migmatites

These rocks occupy more than half of the exposed rocks. Their outcrops occur as uplifted domal old rocks and encompass gneisses, metagabbros-diorites, migmatites, and meta-sedimentary and volcano-sedimentary sequences displaying polyphases of deformations [33]. These rocks are delimited by a complex array of thrust faults trending generally in NE–SW, separating them from folded thrust belts of ophiolitic mélange in the east and metavolcanics in the west. Many authors assigned the ages of these gneisses as pre-Neoproterozoic (> 900 Ma) [34] or Pan-African (900–850 Ma) [35, 36].

2.2 Ophiolitic Mélanges

Ophiolitic mélanges are well exposed in the northeastern and southern parts of the studied province. They occur as E–W elongated exotic blocks embedded in foliated sedimentary matrix [37]. NE–SW and NW–SE-trending folds related to NNW–SSE shortening have been observed [38]. Intraoceanic back-arc to volcanic arc tectonic regime has been proposed for the origin of these rocks [39]. The age of ophiolitic mélange was detected at almost 870–740 Ma [40].

2.3 Island Arc Metavolcanics

These sequences cover ~10% in the western part of the investigated area, uncomfortably overlying the genesis rocks. Metabasalts, metaandesites, metadacites, and their equivalent metapyroclastics with banded iron formation and marble are the main varieties of these volcanic rocks [41]. These rocks are circumscribed by two chief fault thrusts trending in E–W and NNE, plunge toward the NW. Furthermore, in the NW–SE, their trending folds are influenced by penetrating

metamorphism [42]. An age of 813 ± 6 to 615 ± 6 Ma has been assigned to the island arc metavolcanics [43, 44].

2.4 Younger Granites

These rocks are broadly distributed in the investigated region. Their landform forms sharp intrusive contacts with surrounding rock units. They are leucocratic-mesocratic, coarse-grained, red in color, and show compositional range from alkali feldspar granite to syenogranite. Their rocks types enclose numerous xenoliths involving gneissic, ophiolitic, gabbro, and metavolcanic blocks derived from the underlying rocks. The rift-related younger granites have been assigned to 590–550 Ma [45–47].

2.5 Quaternary Deposits

Quaternary deposits are represented by alluvial sediments. The latter are widely distributed in the southern portion of the investigated region such as Wadi Umm Ghalqa, Wadi Haimur, Wadi Bitan, and Wadi Abo Had [48].

Structurally, the examined area is exaggerated by two principal shear zones trending NE and NW. The latter trend is considered as a part of the Najd fault system consisting of a brittle-ductile zone, which has a width of 300 km and extends to 1100 km in length, spreading through the northern portion of the ANS [49, 50]. These shear zones cross the Pan-African ophiolitic mélange, island arc, and numerous intrusive rocks to the east. There are folds and faults, recorded within these shear zones. The former is mainly open asymmetrical anticlines with axial planes striking NE and the limbs dip steeply at about 70° and 60° NW and SE, respectively. These folds mainly plunge more than 80° to the $S40^\circ$ W direction. They mainly affect the island arc metavolcanics and their metapyroclastics (crystal metatuffs) that arise in the northwestern portion of the examined area. Thrust, strike-slip, and normal faults are recorded in the area under investigation, cutting through the ophiolitic mélange and subducted-related volcano-sedimentary rocks (Fig. 1). These faults trend in the ENE–WSW to E–W and dip steeply to the NW. All fault thrusts in the investigated area are analogous to the major axial plane of fold, which happens in the northern part of the area under examination.

3 Data Usability

The aeromagnetic and aero-radio-spectrometric data were obtained over the investigated area among latitudes $22^\circ 45'N$ and $23^\circ 00'N$ and longitudes $33^\circ 50'E$ and $34^\circ 40'E$ by the Aeroservice company [51]. The survey flight lines constructed with spacing of 1000 m between each lines and the tie-lines spacing was 10,000 m perpendicular to flight

lines direction (NE–SW). The attained magnetic and the gamma-ray spectroscopy data are reduced, gathered, and lastly offered in the outline of contour and composite maps.

4 Magnetic Data Processing and Interpretations

The magnetic data were preprocessed and corrected for latitude, diurnal variation, and height issue and the total aerial magnetic map (Tm) of the investigated area was created (Fig. 2). Figure 2 reveals that the Tm-values range from 42,350 to 42,638 nT. Magnetic values can be organized into various colors, as indicated by their amplitudes. First, the blue color shades ranging from 42,350 to 42,420 nT are categorized by low magnetic anomalies, with extended and striking in the NE–SW. The intermediate-scale colors range from 42,420 to 42,500 nT, and mostly cover the southern and the eastern parts. Also, the high amplitude, which ranges from 42,500 to 42,638 nT covers the midpoint of the examined area and strike in the NE–SW trend (Fig. 2).

4.1 Reduced-To-Magnetic Pole (RTP)

Baranov [52] was the first one who introduced reduced-to-magnetic pole (RTP). RTP is an important part of magnetic data processing, especially for large-scale mapping. RTP is intended to remove the skewness of the anomalies and make

it symmetric over the source which is magnetized by induction only, remove influence of magnetic latitude, and reduce the effect of dip magnetization, remove the effect of remnant magnetization. Therefore, the Tm-map (Fig. 2) has an embedded impact of latitude discrepancy because of the dipole of the magnetic field. To decrease this influence, the Tm-data was changed to an unreal position as in the pole of the earth and this permits a good accurateness in the site of the inferred anomalies [52–57].

The RTP-map (Fig. 3) was accomplished relying on the Earth total intensity (42,470 nT), magnetic field inclinations (32.8° N) and declination (1.9° E) of the survey at the location. The RTP-map does not differ completely from the Tm-map, but a few anomalies alter their trend northward through the elimination of the declination of the investigated area (Fig. 3). The magnetic magnitudes in the examined area are circulated intermittently through the lithological variety in the investigated zone and, furthermore, with the manifestation of a sedimentary cover to the south. The RTP-map indicates that the study area is described by an extensive variety of magnetic values ranging from 60 to 185 nT. The RTP highest amplitudes (red shading, which characterized the high magnetic anomalies; RTP-H1 to RTP-H10 zones) are sited in the northern, northwestern, northeastern, and south-southeastern portions and directed to the NE–SW, N–S, and NW–SE trends of the inspected area. Likewise, the lowest values (blue shading, which characterized the low magnetic anomalies;

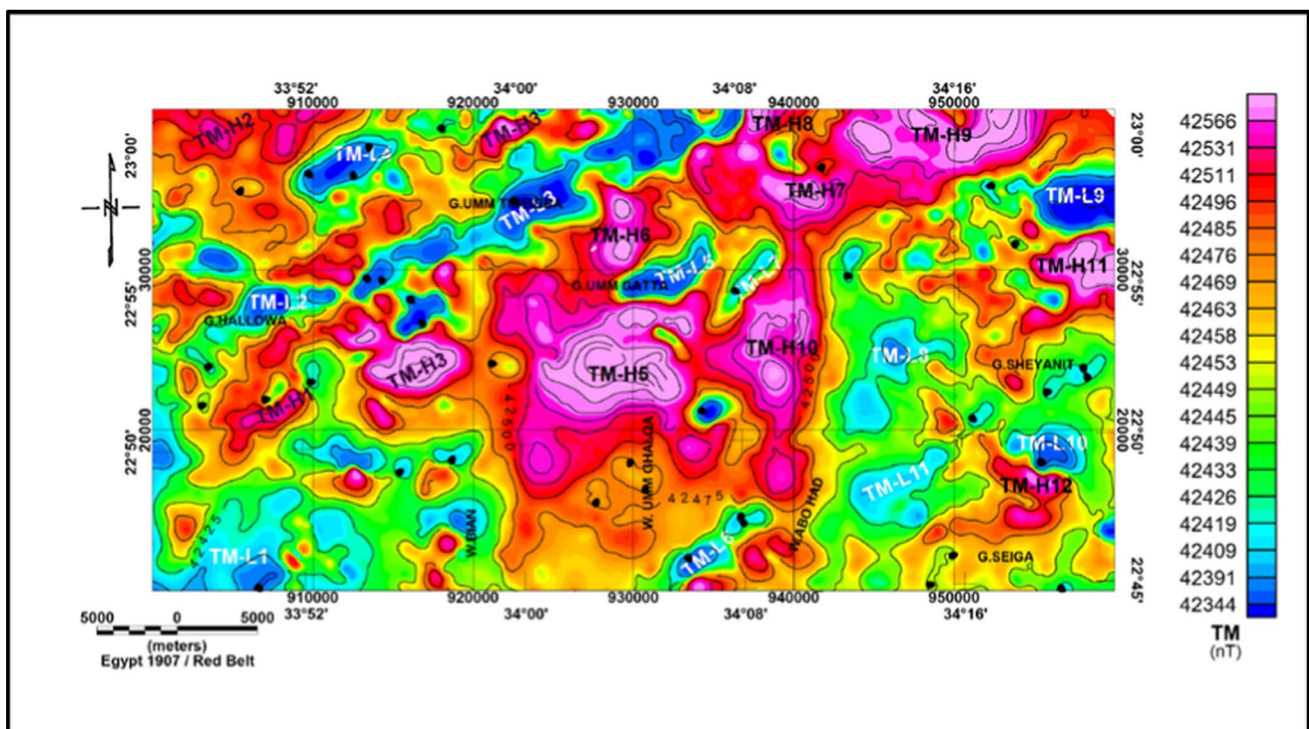


Fig. 2 The total magnetic (Tm) map of Umm Tineidba area, Southern Eastern Desert, Egypt [51]

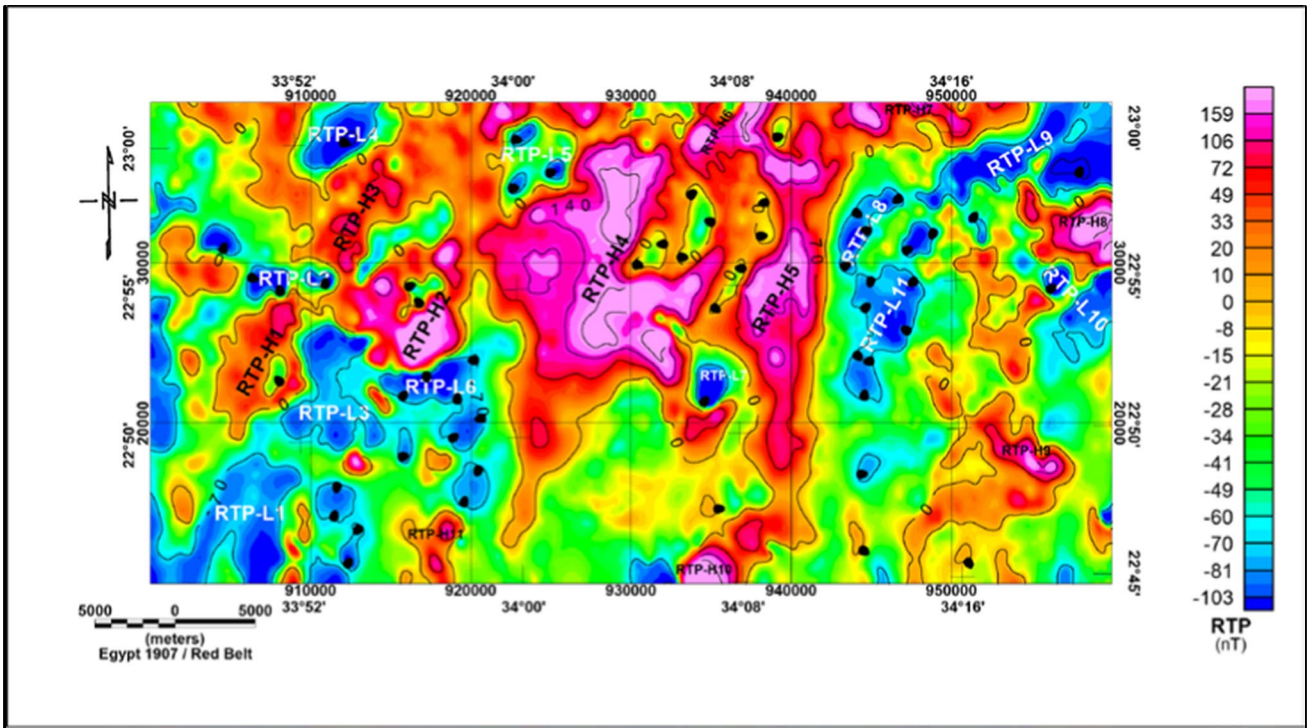


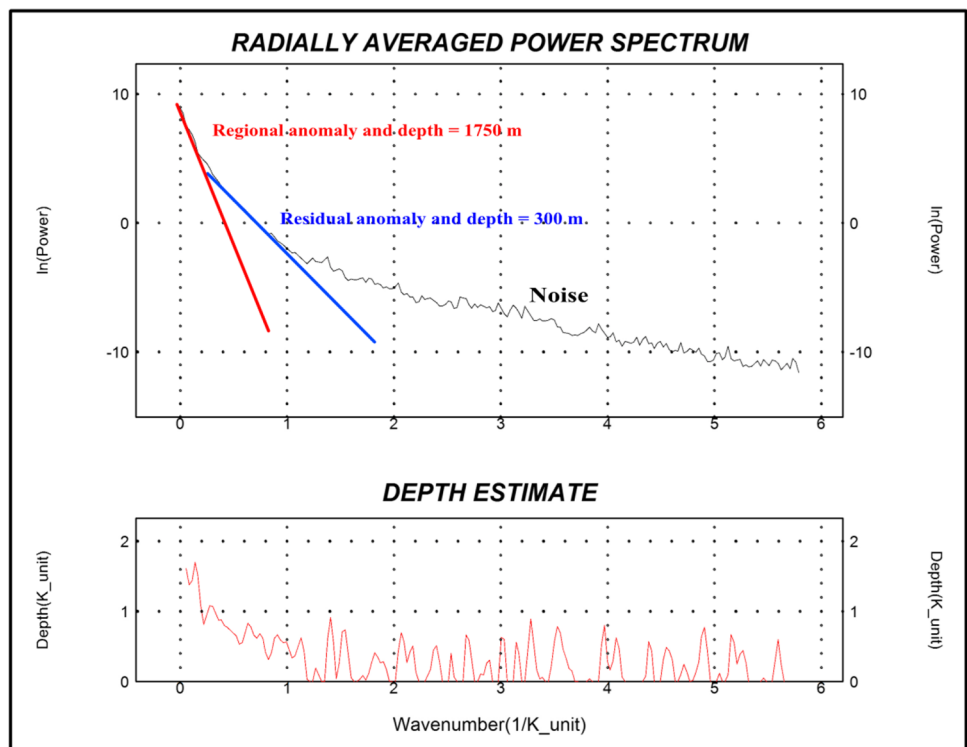
Fig. 3 The reduced-to-pole aeromagnetic (RTP) map of Umm Tineidba area, Southern Eastern Desert, Egypt

RTP-L1 to RTP-L11 zones) of -75 to -110 nT reading are found in the northeastern, southwestern, and northwestern parts and striking in the NE–SW directions in the area under study.

4.2 Power Spectrum (PS)

The power spectrum (PS) method was utilized to segregate the local (residual) and global (regional) magnetic fields,

Fig. 4 The power spectrum curves of the reduced-to-pole aeromagnetic (RTP)-map of Umm Tineidba area, Southern Eastern Desert, Egypt



detect the depths of shallow and deeper structures, and delineate subsurface geologic structures [58–61]. This method uses the fast Fourier transform. Therefore, a 2D power spectrum curve was attained (Fig. 4). The slopes of the portions yielding the depth evaluation for magnetic sources were calculated. The depth (z) for every source outfit in charge of each segment was figured by presenting the slope of this part in the formula:

$$z = \frac{-slope}{4\pi}. \quad (1)$$

Moreover, the depth is evaluated from the slope of the plot between the logarithmic power spectrum and wave-number (Fig. 4). The radially averaged power spectrum of the magnetic spectrum can be interpreted as two linear slope segments and has been applied to estimate the depth of magnetic interface at 1750 m and 300 m, which represent the average depth to the lower and upper surface of the magnetized body (Fig. 4). Also, the residual and regional magnetic maps, which represent the near-surface and deep-seated structures, were presented by implementing the power spectrum procedure on the aeromagnetic map (Figs. 5 and 6, respectively). Figure 5 exhibits the residual magnetic map, which lacks the subterranean crustal inhomogeneity, and shows various positive and negative anomalies, and some of them are striking in the NE–SW direction (majority), as well as N–S and NW–SE. Also, the high magnetic values

are given in Fig. 5 (RES-H) and values range between 10 and 54 nT. In contrast, the lower values are represented by symbol RES-L and range from –20 to –55 nT. Meanwhile, Fig. 6 shows the regional magnetic map and map portrays the main subsurface patterns that influence the deep-seated structures and their depths vary between 300 and 1750 m. This map describes two main sets of structures trending in the NE–SW and NNE–SSE, which represent the highest regional anomalies (REG-H1 to REG-H8) and their values range from 60 to 145 nT while the lowest regional anomalies values (REG-L1 to REG-L9) range from –63 to –90 nT (Fig. 6). Even as these patterns are overwhelming on this map, the nearness of the short NW–SE and E–W trending faults are likewise significant.

4.3 3D Analytical signal (A_s)

Magnetic elucidation was achieved utilizing an adapted method, established totally on the simplification of the analytical signal (A_s technique) in 3D. Roset et al. [62] precisely defined the absolute amplitude value of the 3D analytical signal as follows:

$$A_s = \sqrt{(THDR)^2 + (VDR)^2}, \quad (2)$$

where $VDR = -\frac{\partial T}{\partial z}$ is the vertical derivative of the magnetic field in the direction of z and

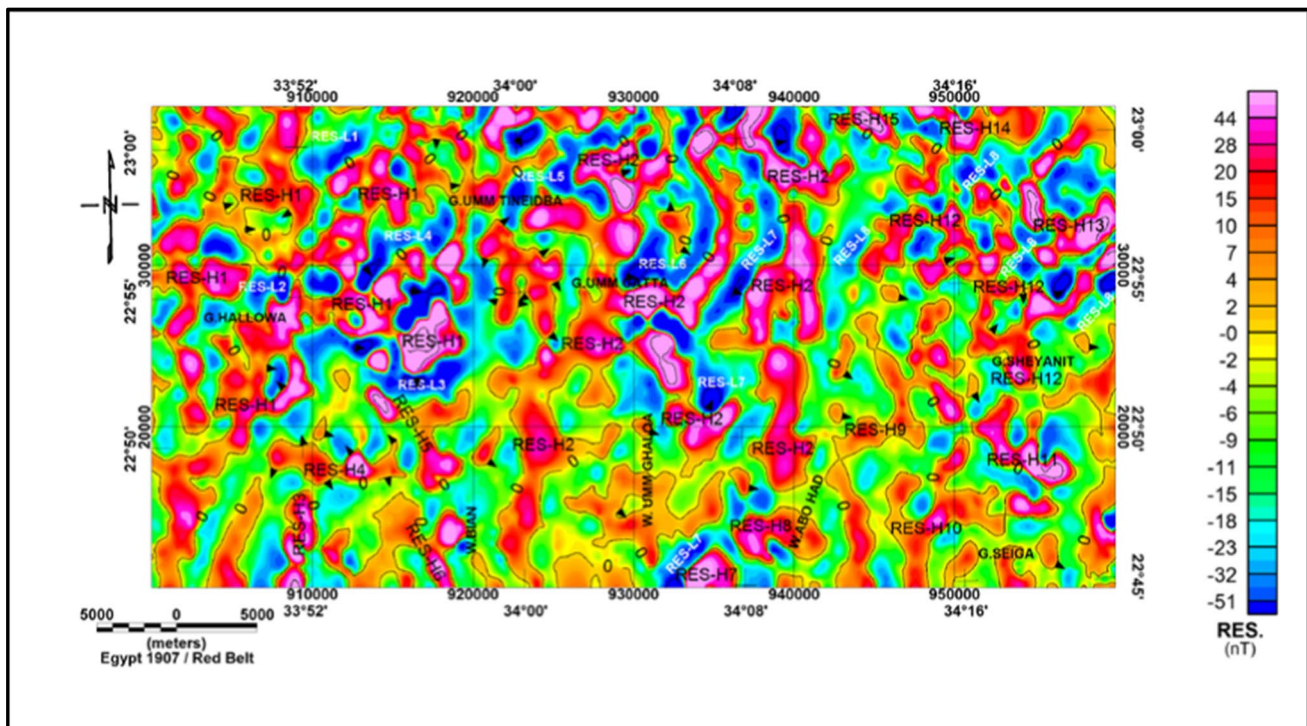


Fig. 5 Residual aeromagnetic anomaly map of Umm Tineidba area, Southern Eastern Desert, Egypt, and the black lines represent the interpreted lineament trends

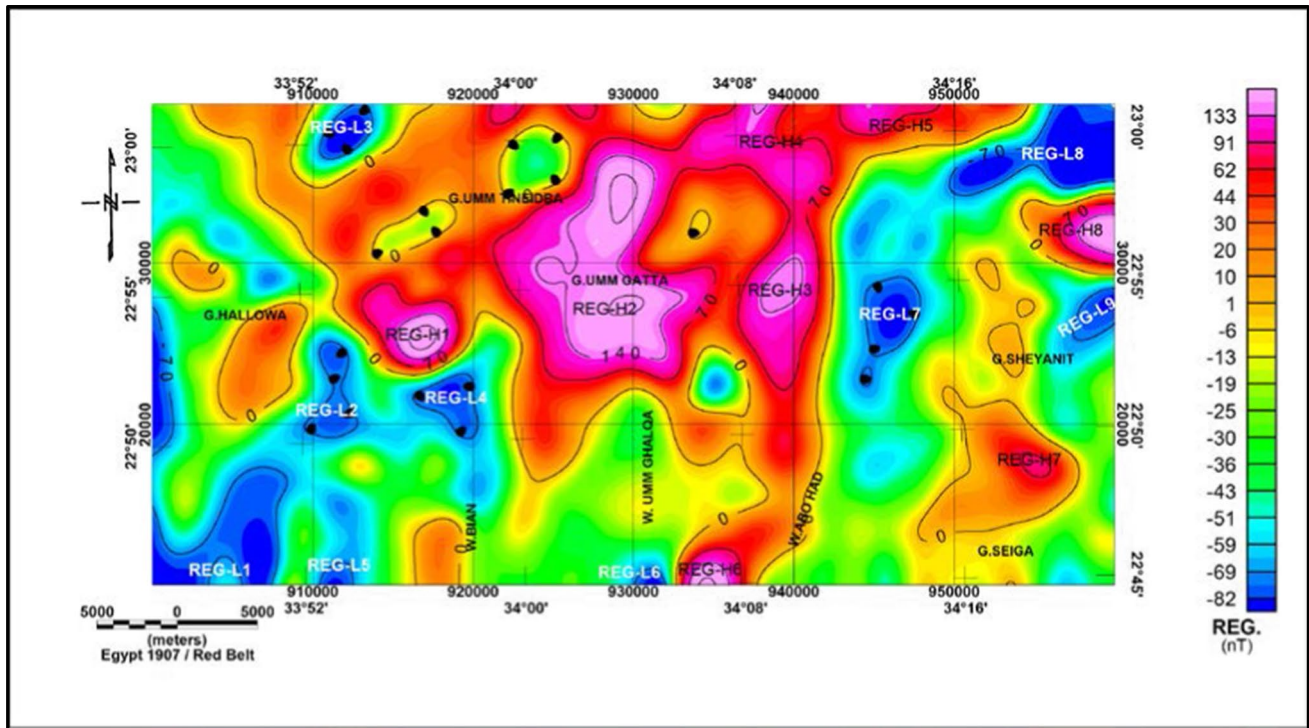


Fig. 6 Regional aeromagnetic map of Umm Tineidba area, Southern Eastern Desert, Egypt, and the black lines represent the interpreted lineament trends

$$THDR = \sqrt{\left(\frac{\partial T}{\partial x}\right)^2 + \left(\frac{\partial T}{\partial y}\right)^2}, \tag{3}$$

is the total horizontal derivative of the magnetic field in the direction of x and y.

The analytical signal process is valuable in finding the boundaries of the magnetic field [63]. The benefit of utilizing the As-technique is to decide magnetic constraints from magnetic abnormalities. These include the freedom of magnetization inclination, less delicate noise in the data and interfering impact among shallow sources. Similarly, this change was regularly valuable at low magnetic latitudes, e.g., the investigated part [64]. Figure 7 reveals the As-map of the aeromagnetic data. This map designates that the high-values (AS-H) were detected at the northern, northwestern, northeastern, which indicated that these regions have significant magnetic contrasts that produce recognizable signatures (red colors) and few peak-values at the south and southeastern sides of the investigated area. The lineaments patterns resulting from this map are in the NE–SW, N–S, NW–SE, N–S, and E–W trends. Also, lower esteems of the As tendencies in the NE–SW and NW–SE are detected at numerous positions in the northern and south-central portions of the examined region.

4.4 Tilt angle (Tg)

Miller and Singh [65] anticipated the tile-angle (Tg) as:

$$Tg = \tan^{-1}\left(\frac{-VDR}{THDR}\right). \tag{4}$$

The tilt angle (Tg) values have the property of presence (+) over a magnetized source, fleeting during zero at the verge of a vertical-sided cause, and (–) esteem somewhere else (Miller and Singh 1994). A vital feature of the Tg is that the amplitudes of robust and frail anomalies can be adjusted adequately, enabling anomalies to be sketched out along-strike while generally ignoring the depth of the source [55, 65, 66]. Because of this, the Tg has an identical characteristic for various depth source and is capable of coming across the limits of the shallower and deeper sources. Verduzco et al. [63] have shown that the Tg-values are confined to values among $+\pi/2$ and $-\pi/2$ ($+90^\circ$ and -90°) due to the natural property of the inverse tangent function. This information makes computing the Tg comparable to an automatic gain control filter. Also, the delineation of the depth to the vertical contact can be estimated from the half-distance between $+\pi/4$ and $-\pi/4$ [66].

Figure 8 illustrates that the projection of the magnetic field source focuses on the ground, is the fundamental

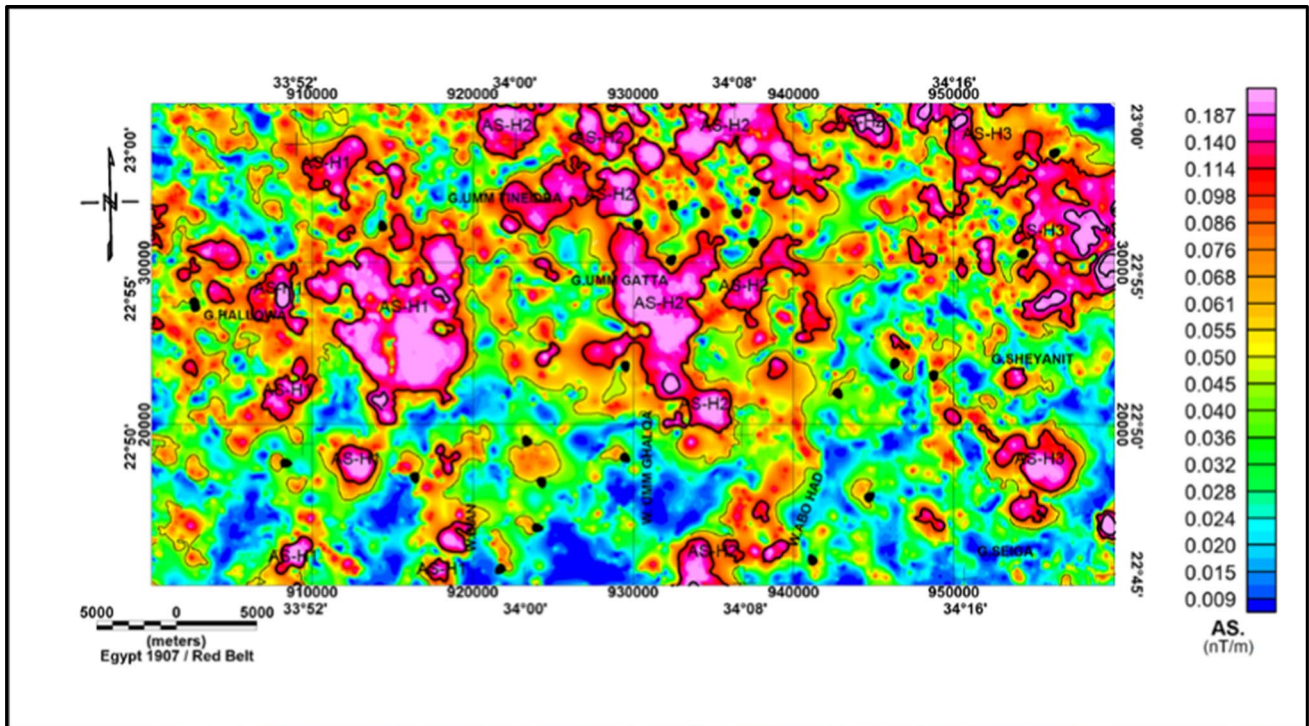


Fig. 7 The 3D analytical signal (As) map of Umm Tineidba area, Southern Eastern Desert, Egypt

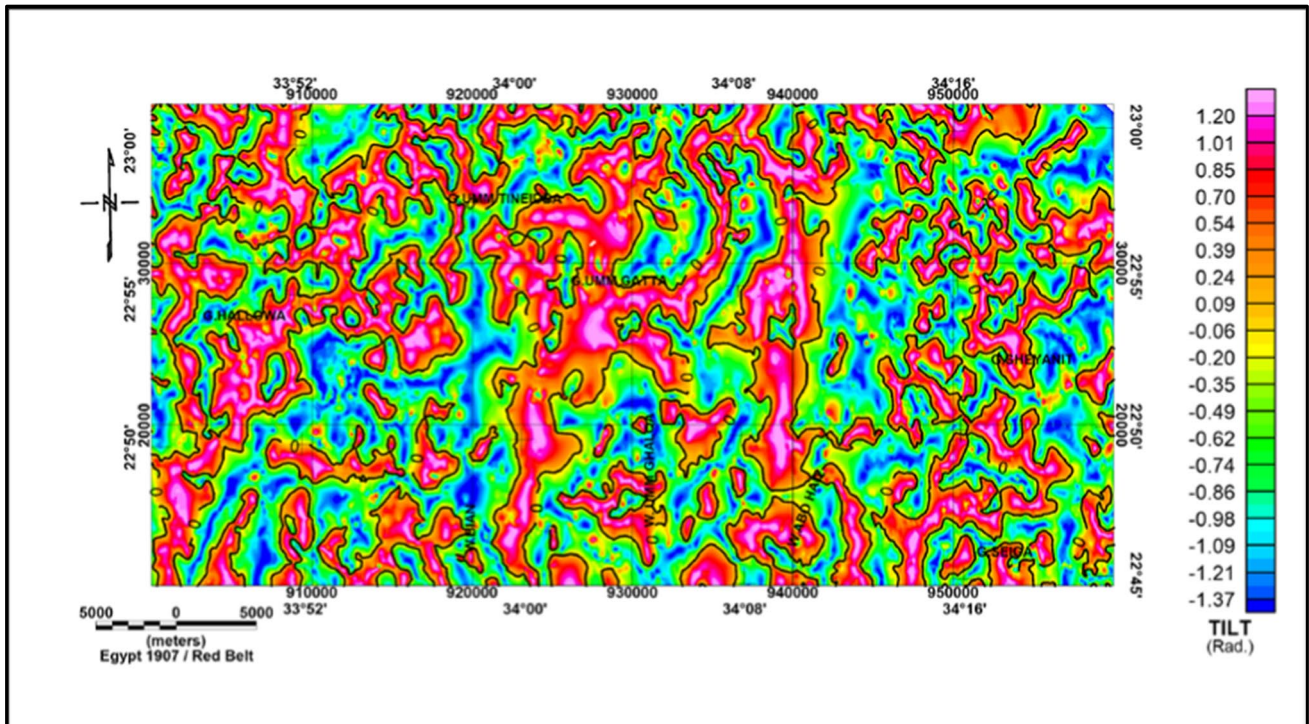


Fig. 8 The tilt angle (Tg) map applied on the RTP-map of Umm Tineidba area, Southern Eastern Desert, Egypt

dissemination in the Precambrian rocks, and also reveals that the zero relief path is sited near the fault interaction. The interpretation of the Tg map, applied on the RTP-map,

outlines the changes anomalies between positive (orange and red colors) and negative values (yellow to blue colors), which demonstrate the alignment of anomalies. The Tg-map

produces fully elongated zones and takes the NE–SW, NNE–SSW, NE–SW, and N–S trend directions.

4.5 Local Wavenumber (LW)

The LW arises from the source parameter imaging technique [67], which evaluated the depth from the LW of the analytic signal. The $K(x, y)$ gives the precise amount of modification of the local phase of the total-field of the horizontal (x and y) directions and simplified as:

$$K(x, y) = \frac{\frac{\partial^2 T}{\partial x \partial z} T_x + \frac{\partial^2 T}{\partial y \partial z} T_y + \frac{\partial^2 T}{\partial z^2} T_z}{(As)^2}, \tag{5}$$

where T_x , T_y , and T_z are the byproducts in x , y , and z -directions of the total-field. For contact, the maximum values of K are placed straight above the contact edges and liberated on the magnetic inclination, declination, dip, direction, and any vestige of magnetization. The interference is reduced due to using the 2nd-order imitative of the magnetic arena. The depth is appraised at the source edges from the following equation:

$$Depth = \frac{1}{K_{max}}, \tag{6}$$

where K_{max} is the extreme value of the LW and above the edge source.

Figure 9 shows the depth evaluation using the LW technique and demonstrates the depth ranges for the shallow structure is extended up to 350 m and for deeper structure lie between 400 and 1200 m.

5 Spectrometric Data Application

The gamma-ray spectroscopy data analysis purposes to localize anomalies, which include the uranium ores that could be correlated with lithology units and mineralization. However, the radiometric technique is best effective in regions controlled by the progressed intrusion, where the radioactive component deliberations are usually greater and revealed in a wide-range of various geologic settings. For example, massive sulfide and gold ores are commonly in the form of sericite [30].

Figure 10 demonstrated the whole amount of the gamma radiation (T_c in $\mu R/h$) that point to three zones (differentiated by three different colors) founded in the examined region. The first one (Z_1) in the middle of the area under investigation (Quaternary deposits and ophiolitic basic meta-volcanic) trends N–S has a low radiometric concentration ($\leq 4 \mu R/h$). The second zone (Z_2) is the intermediate region (4 to 7 $\mu R/h$) and mainly recorded over pre-Neoproterozoic or disinterred Neoproterozoic rocks and covered more than 50% of the study region. Finally, the third zone (Z_3) (≥ 7

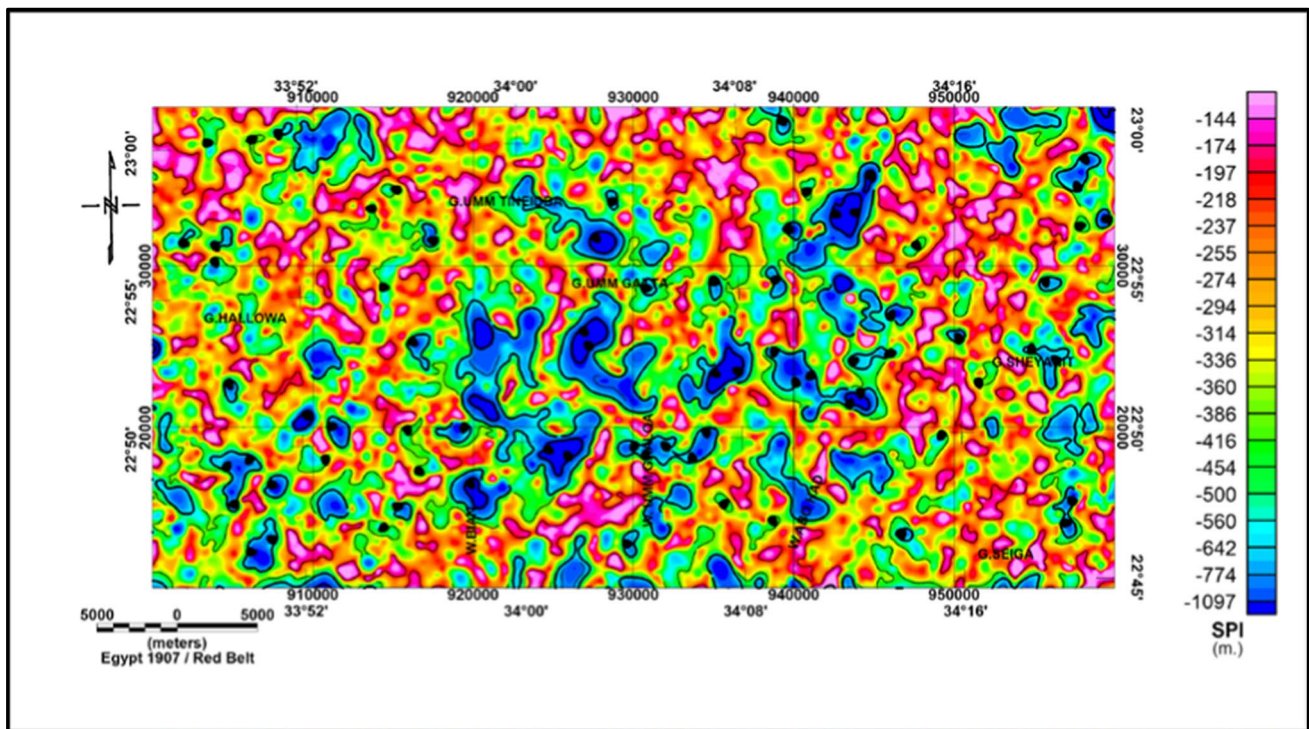


Fig. 9 The depth estimates using the local wave number (LW) technique of Umm Tineidba area, Southern Eastern Desert, Egypt

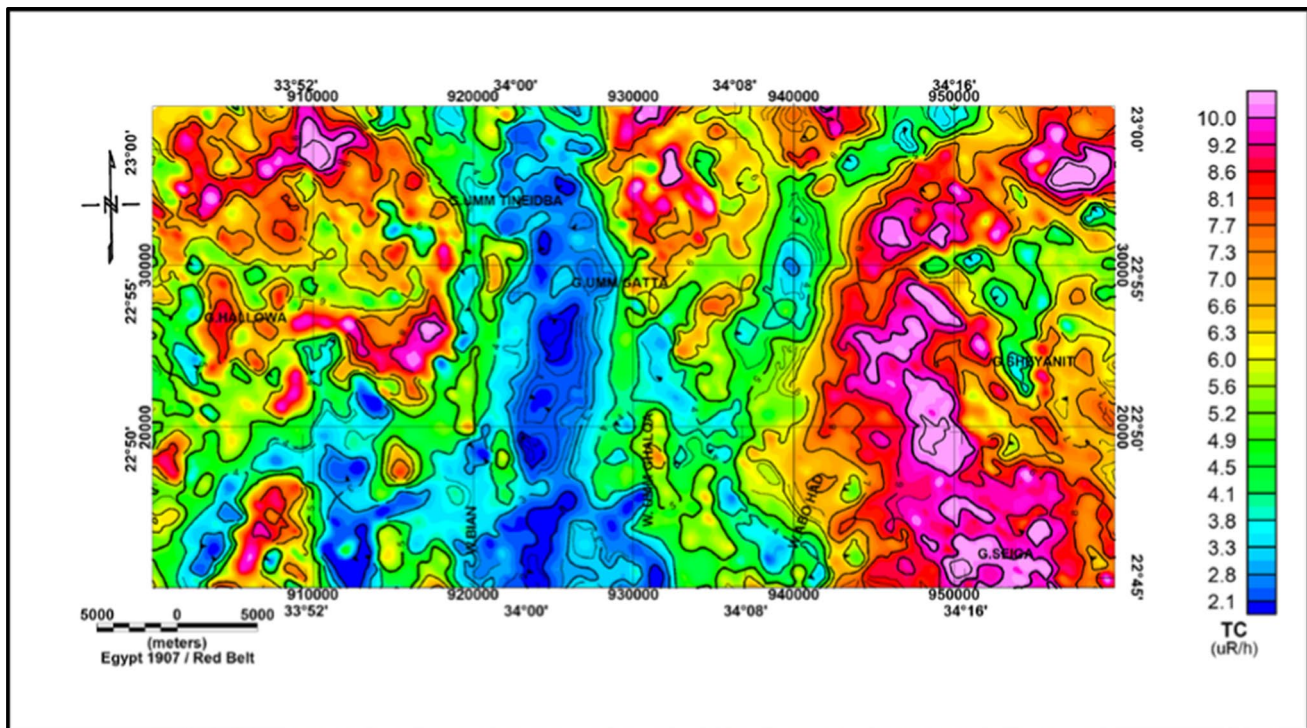


Fig. 10 The total-count (Tc) of the Umm Tineidba area, Southern Eastern Desert, Egypt

$\mu\text{R/h}$) is recorded over the granitic and metamorphosed rocks at the eastern part from N–S and in the NW part.

Furthermore, Fig. 11 demonstrates the elucidated point anomaly map of the area under investigation, which possesses values exceeding $X + 2S$ for eU, eU/eTh, and eU/K variables. Various anomalous points were distinguished on this map [48]. The aero-radio-spectrometric maps show a wide record at different levels of rock protrusions and are controlled by the geological history of the examined area. Transitory explanations of the qualitative interpretation of the identified aero-radio-spectrometric maps with the characteristic rock suites are shown in Table 1.

6 Results and Discussions

The trends of the interpreted features resulted from the residual and provincial maps are incorporated with the results from As and Tg methods (Fig. 12). Moreover, using airborne gamma ray spectrometric and different magnetic elucidation methods (As, Tg, for the RTP-map) help to determine the different locations of the main anomalies. So, the analysis of aeromagnetic lineaments from the residual and regional magnetic maps revealed the dominant trends include NE–SW and NNE–SSW and the subordinate ones comprise the N–S and E–W guidelines (Fig. 12) The dominant NE–SW trends were detected by Abdel Hafeez [48] and Essa [30]

in their studies. The NE–SW trend is associated with the shear zones crossing the Pan-African belt, whereas the E–W patterns are the products of the pre-Pan-African belt. The basement depths of magnetic sources from the RTP-magnetic map using the PS and the LW techniques are shown on the area (Table 2). Table 2 reveals that the depth of shallow structures extended up to 400 m and the depth of the deeper structure is also extended up to 1750 m. In addition, the increased percent of U-values in the Quaternary sediments places refer to leaks and migration from the granite to the wadis. This phenomenon is due to the migration and ascending of the deep hydrothermal fluids along the fault zones.

6.1 Joint Interpretation of Available Data to Delineate Mineralized Zones

The magnetic and γ -spectrometric data display that the investigated region is exaggerated by severe tectonic deformations. The metagabbro and metadiorite rocks are categorized by numerous high magnetic anomalies, especially in the central part of the investigated area. The sheared hydrothermal deposits involving uranium, gold, and sulfide mineralization were intensively rehabilitated and by the later faults-controlled magmatic activity. These ore deposits show high magnetic anomalies near their boundaries and close

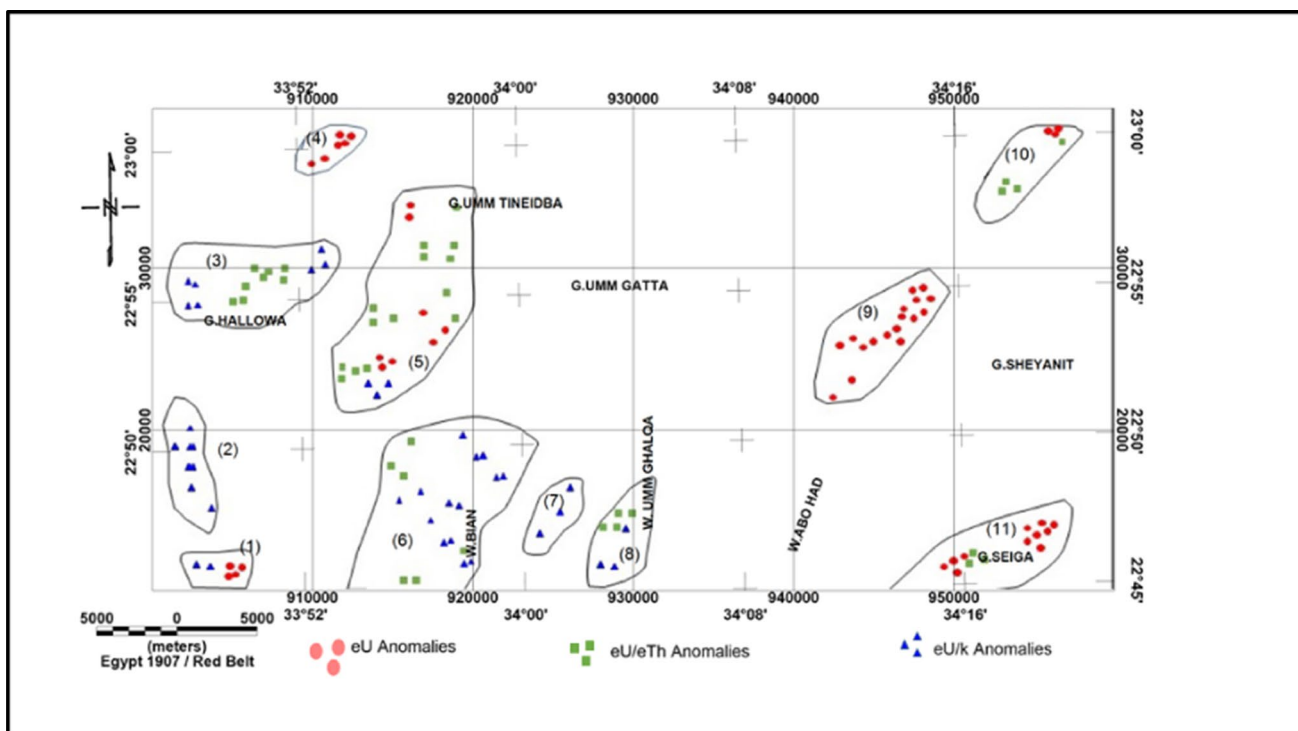


Fig. 11 Point anomaly map of the Umm Tineidba area, Southern Eastern Desert, Egypt [48]

to the younger granite and gneisses/migmatites along the structural lineaments and faulted zones (Fig. 12). The Umm Tineidba area and its environs show that their ore deposits have significant regional magnetic highs, which reflect that the durable magmatic activity could deliver respectable sources for the formation of diverse metallogenic systems. The latter are controlled by the NE and NW trending structures and their deep hydrothermal fluids deliver a good indication for gold mineralization. Therefore, the NE- and NW-trending

shear zones were the main controlling structures, which facilitate the mineralizing magmatic ascent in the study area.

7 Conclusions

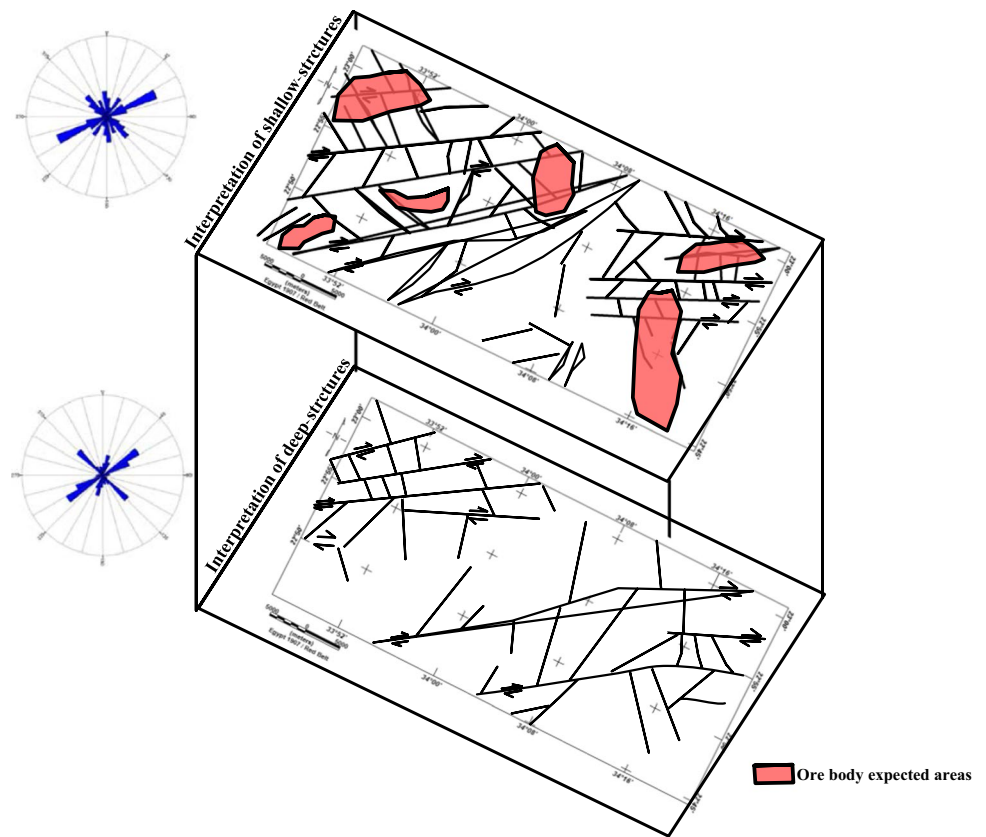
The objectives of this study included applying the available aeromagnetic and aero-spectrometric data for delineating and locating the sources that contain

Table 1 Qualitative radio-spectrometric explanation for the main geologic units in the study area

Rock unit	Tc (Ur) level (m)	Position	Place (Fig. 1)
Gneisses and migmatites	I (6–8)	70% of study area	Gabel Hallowa, Gabel Umm Tineidba, Gabel Umm Gatta, N. of Gabel Sheiyanit, E. of Gabel Seiga, some parts in Wadi Abo Had, Wadi Umm Ghalqa, Wadi Biam and Wadi Haimur
Ophiolitic mélanges	I (7–8.5)	NE, S, SW of the study area	N. of Gabel Sheiyanit, E. of Wadi Umm Ghalqa, W. of Gabel Nusb Aloba
Island arc metavolcanic	I (4–6)	W. of the study area	W. of Gabel Hallowa
Younger granites	H (< 9)	NE, SE, NNW, SSW, S of the study area	N. of Gabel Sheiyanit, Gabel Seiga, Gabel Abo Gharatif, Gabel Nusb Aloba, Gabel Umm Krush
Quaternary deposits	L (< 3)	Middle of the study area	Wadi Haimur, Wadi Umm Ghalqa, Wadi Abo Had, Wadi Biam

Abbreviations: Tc (total count), H (high), I (intermediate), L (low), N (north), S (south), E (east), W (west)

Fig. 12 Interpreted structures and mineralized zones of the Umm Tineidba area, Southern Eastern Desert, Egypt



minerals deposits involving uranium, gold, and sulfide and the trend of the control lineament structures in the Gebel Umm Tineidba and its surroundings, Egypt. The total intensity (Tm) map, total count (Tc) map, and geological information of the study area were delineated. Ophiolitic mélanges sequences (serpentinites, gabbros, basic pillow volcanic) were delineated by a high magnetized source that is highly enriched in radioactive minerals (uranium, gold, and sulfide deposits) located by the Tm- and the RTP-maps. After a careful elucidation applying the power spectrum (PS), analytic signal (As), tilt angle (Tg), and local wavenumber (LW) methods, the study area has a multifaceted design of long and short wavelengths forming magnetic signatures that are inherited in Precambrian basement rocks. The

pattern of total-intensity magnetic map reflects that the ore deposits are localized along the dominant trend of NE–SW and N–S with minor E–W and NW–SE lineament structures. The N–S, NE–SW, and NW–SE linear structures are related to Pan-African orogeny, whereas the E–W trend is to pre-Pan-African orogeny. Depth evaluations from PS and LW techniques publicized a dual layer deep and shallow (from 1750 to 400 m) depth source. The expected area for mineral and ores zones (Fig. 12) should be further studied to ensure our results.

Acknowledgements The authors would like to thank Prof. Ronel Kappes, Executive Editor, Prof. Virginia McLemore, Editor-in-Chief, and the two capable reviewers for their keen interest, valuable comments on the manuscript, and improvements to this work.

Author Contributions All authors contributed to the design and implementation of the research, to the analysis of the results and to the writing of the manuscript.

Funding Open access funding provided by The Science, Technology & Innovation Funding Authority (STDF) in cooperation with The Egyptian Knowledge Bank (EKB).

Data Availability The used datasets are available upon request from the corresponding author.

Code Availability Not applicable.

Table 2 The interpreted results for the investigation area using the power spectrum (PS) technique and the local wavenumber (LW) technique

The method	Depth for the shallow structure (m)	Depth for the deep structure (m)
The PS-technique	extended up to 400	400–1750
The LW-technique	extended up to 350	350–1200

Declarations

Conflict of Interest The authors declare that they have no competing interests.

Open Access This article is licensed under a Creative Commons Attribution 4.0 International License, which permits use, sharing, adaptation, distribution and reproduction in any medium or format, as long as you give appropriate credit to the original author(s) and the source, provide a link to the Creative Commons licence, and indicate if changes were made. The images or other third party material in this article are included in the article's Creative Commons licence, unless indicated otherwise in a credit line to the material. If material is not included in the article's Creative Commons licence and your intended use is not permitted by statutory regulation or exceeds the permitted use, you will need to obtain permission directly from the copyright holder. To view a copy of this licence, visit <http://creativecommons.org/licenses/by/4.0/>.

References

- Abdelrahman EM, Soliman KS, El-Araby TM, Abo-Ezz ER, Essa KS (2009) A least-squares standard deviation method to interpret magnetic anomalies due to thin dikes. *Near Sur Geophys* 7:41–46
- Akbar S, Fathianpour N (2016) Improving the Curie depth estimation through optimizing the spectral block dimensions of the aeromagnetic data in the Sabalan geothermal field. *J Appl Geophys* 135:281–287
- Farhi W, Boudella A, Saibi H, Bounif M (2016) Integration of magnetic, gravity, and well data in imaging subsurface geology in the Ksar Hirane region (Laghout, Algeria). *J Afr Earth Sci* 124:63–74
- Deng Y, Chen Y, Wang P, Essa KS, Xub T, Liang X, Badal J (2016) Magmatic underplating beneath the Emeishan large igneous province (South China) revealed by the COMGRA-ELIP experiment. *Tectonophysics* 672–673:16–23
- Essa KS, Abo-Ezz ER (2021) Potential field data interpretation to detect the parameters of buried geometries by applying a nonlinear least-squares approach. *Acta Geodyn Geophys* 56:387–406
- Gavazzi B, Alkhatib-Alkontar R, Munsch M, Colin F, Duvette C (2017) On the use of fluxgate 3-axis magnetometers in archaeology: application with a multi-sensor device on the site of Qasr 'Allam in the Western Desert of Egypt. *Archaeol Prospect* 24:59–73
- Essa KS, Elhussein M (2018) PSO (Particle Swarm Optimization) for Interpretation of Magnetic Anomalies Caused by Simple Geometrical Structures. *Pure Appl Geophys* 175:3539–3553
- Le Maire P, Munsch M (2018) 2D Potential field theory using complex algebra: new equations and visualization for the interpretation of potential field data. *Geophysics* 83:J1–J13
- Arinze IJ, Emedo CO (2021) Integrated Geophysical Investigation for Shallow-Scale Massive (Pb-Zn) Sulphide and Barite Exploration in the Abakaliki and Obubra Mining Districts (AOMD), Southeastern Nigeria. *Min Metall Explor* 38:381–395
- Essa KS, Elhussein M (2020) Interpretation of magnetic data through particle swarm optimization: Mineral exploration cases studies. *Nat Resour Res* 29:521–537
- Mehanee S, Essa KS, Diab ZE (2021) Magnetic data interpretation using a new r -parameter imaging method with application to mineral exploration. *Nat Resour Res* 30:77–95
- Nabighian MN, Grauch VJS, Hansen RO, LaFehr TR, Li Y, Peirce JW, Phillips JD, Ruder ME (2005) The historical development of the magnetic method in exploration. *Geophysics* 70:33ND–61ND
- Mandal A, Biswas A, Mittal S, Mohanty WK, Sharma SP, Sen-gupta D, Sen J, Bhatt AK (2013) Geophysical anomalies associated with uranium mineralization from Beldih Mine, South Purulia Shear Zone, India. *J Geol Soc India* 82:601–606
- Abdelrahman EM, Essa KS (2015) A new method for depth and shape determinations from magnetic data. *Pure Appl Geophys* 172:439–460
- Abo-Ezz ER, Essa KS (2016) A least-squares minimization approach for model parameters estimate by using a new magnetic anomaly formula. *Pure Appl Geophys* 173:1265–1278
- Abdelrahman EM, El-Araby HM, El-Araby TM, Essa KS (2003) A least-squares minimization approach to depth determination from magnetic data. *Pure Appl Geophys* 160:1259–1271
- Abdelrahman EM, Abo-Ezz ER, Essa KS, El-Araby TM, Soliman KS (2007) A new least-squares minimization approach to depth and shape determination from magnetic data. *Geophys Prospect* 55:433–446
- Mattsson HB, Balashova A, Almqvist BSG, Bosshard-Stadlin SA, Weidendorfer D (2018) Magnetic mineralogy and rock magnetic properties of silicate and carbonatite rocks from Oldoinyo Lengai volcano (Tanzania). *J Afr Earth Sci* 142:193–206
- Abdelrahman EM, Abo-Ezz ER, Essa KS (2012) Parametric inversion of residual magnetic anomalies due to simple geometric bodies. *Explor Geophys* 43:178–189
- Essa KS, Elhussein M (2017) A new approach for the interpretation of magnetic data by a 2-D dipping dike. *J Appl Geophys* 136:431–443
- Moghaddam MM, Mirzaei S, Nouraliee J, Porkhial S (2016) Integrated magnetic and gravity surveys for geothermal exploration in Central Iran. *Arab J Geosci* 9:506
- Oladunjoye MA, Olayinka A, Alaba M, Adabanija MA (2016) Interpretation of high resolution aeromagnetic data for lineaments study and occurrence of Banded Iron Formation in Ogbomoso area, Southwestern Nigeria. *J Afr Earth Sci* 114:43–53
- Abedi M (2018) An integrated approach to evaluate the Aji-Chai potash resources in Iran using potential field data. *J Afr Earth Sci* 139:379–391
- Essa KS, Nady AG, Mostafa MS, Elhussein M (2018) Implementation of potential field data to depict the structural lineaments of the Sinai Peninsula, Egypt. *J Afr Earth Sci* 147:43–53
- Elhussein M, Shokry M (2020) Use of the airborne magnetic data for edge basalt detection in Qaret Had El Bahr area, Northeastern Bahariya Oasis, Egypt. *Bull Eng Geol Environ* 79:4483–4499
- Stern RJ (1994) Arc assembly and continental collision in the Neoproterozoic East African Orogen: Implications for the consolidation of Gondwanaland. *Annu Rev Earth Planet Sci* 23:319–351
- Johnson PR, Kattan FK, Al-Saleh AM (2004) Neoproterozoic ophiolites in the Arabian shield: field relations and structure. In: Kusky TM (Ed.), *Precambrian Ophiolites and Related Rocks*. *Dev Precambrian Geol* 13:129–162
- Kusky TM, Abdelsalam M, Tucker R, Stern RJ (2003) Evolution of the East African and related Orogens, and the assembly of Gondwana. *Precambrian Res* 123:81–344
- El Gaby S (2009) Tectonic evolution of the Pan-African Belt in Egypt. *Bull Tethys Geol Soc* 4:1–8
- Essa WH (2015) Analysis and interpretation of airborne magnetic and gamma-ray spectrometric survey data of Gabel Umm Tineidba aream South Eastern Desert, Egypt. M.Sc. Thesis, Al-Azhar University
- Ali KA, Andresen A, Stern RJ, Manton WI, Omar SA, Maurice AE (2012) Composition, age, and origin of the ~620 Ma Humr

- Akarim and Humrat Mukbid A-type granites: no evidence for pre-Neoproterozoic basement in the Eastern Desert, Egypt. *Int J Earth Sci* 101:1705–1722
32. Johnson PR, Halverson G, Kusky T, Stern R, Pease V (2013) Volcanosedimentary basins in the Arabian-Nubian shield: markers of repeated exhumation and denudation in a Neoproterozoic Accretionary Orogen. *Geosciences* 3:389–445
 33. Greiling RO, Abdeen MM, Dardir AA, El Akhal H, El Ramly MF, Kamal El Din GM, Osman AF, Rashwan AA, Rice AH, Sadek MF (1994) A structural synthesis of the Proterozoic Arabian-Nubian Shield in Egypt. *Geol Rund* 83:484–501
 34. Khudeir AA, Abu El-Rus MA, El-Gaby S, El-Nady O, Bishara WW (2008) Sr-Nd isotopes and geochemistry of the infrastructural rocks in Meatiq and Hafafit core complexes, Eastern Desert, Egypt: Evidence for involvement of pre-Neoproterozoic crust in the growth of Arabian-Nubian Shield. *Isl Arc* 17:90–108
 35. Andresen A, Augland LE, Boghdady GY, Elnady OM, Lundmark AM, Hassan MA, Abu El-Rus MA (2010) Structural constraints on the evolution of the Meatiq Gneiss Dome (Egypt), East African Orogen. *J Afr Earth* 57:413–422
 36. Lundmark AM, Andresen A, Hassan MA, Augland LE, Abu El-Ru MA, Boghdady GY (2012) Repeated magmatic pulses in the East African Orogen of Central Eastern Desert, Egypt: an old idea supported by new evidence. *Gondwana Res* 22:227–237
 37. Ali-Bik MW, Taman Z, El Kalioubi B, Abdel Wahab W (2012) Serpentine-hosted talc–magnetite deposits of Wadi Barramiya area, Eastern Desert, Egypt: characteristics, petrogenesis and evolution. *J Afr Earth Sci* 64:77–89
 38. Ries AC, Shackleton RM, Graham RH, Fitches WR (1983) Pan African structures, ophiolites and melange in the Eastern Desert of Egypt: a traverse at 268N. *J Geol Soc Lond* 140:75–95
 39. El Bahariya G (2012) Classification and origin of the Neoproterozoic ophiolitic mélanges in the Central Eastern Desert of Egypt. *Tectonophysics* 568–569:357–370
 40. Stern RJ, Johanson PR, Krøner A, Yibas B (2004) Neoproterozoic ophiolites of the Arabian–Nubian Shield. In: Kusky, T.M. (Ed.), *Precambrian Ophiolites and Related Rocks*. Developments in Precambrian Geology 13:95–128
 41. Abu El-Ela FF (1997) Geochemistry of an island-arc volcanic suite: Wadi Dabr intrusive complex, Eastern Desert, Egypt. *J Afr Earth* 24:473–496
 42. El-Bialy MZ (2010) On the Pan-African transition of the Arabian-Nubian shield from compression to extension: the post-collision Dokhan volcanic suite of Kid-Malhak region, Sinai, Egypt. *Gondwana Res* 17:26–43
 43. Bielski M (1982) Stages in the evolution of the Arabian Nubian massif in Sinai, Egypt. PhD Thesis, Hebrew University, Jerusalem, p 155
 44. Moghazi AM, Ali K, Wilde SA, Zhou Q, Andersen T, Andersen A, Abu-El Enen M, Stern RJ (2012) Geochemistry, geochronology, and Sr–Nd isotopes of the Late Neoproterozoic Wadi Kid volcano-sedimentary rocks, Southern Sinai, Egypt: implications for tectonic setting and crustal evolution. *Lithos* 154:147–165
 45. Hussein AA, Aly MM, El Ramly MF (1982) A proposed new classification of the granites of Egypt. *J Volcanol Geoth Res* 14:187–198
 46. Hassan MA, Hashad AH (1990) Precambrian of Egypt. In: Said, R. (Ed.), *The geology of Egypt*. A.A. Balkema, Rotterdam, Netherlands, pp 201–245
 47. Gahlan HA, Azer MK, Asimow P, Al-Kahtany K (2016) Late Ediacaran post-collisional a-type syenites with shoshonitic affinities, northern Arabian-Nubian Shield: a possible mantle-derived a-type magma. *Arab J Geosci* 9:603
 48. Abdel Hafeez TH (2015) Interpretation of airborne magnetic survey of Gabel Um Tineidba area, south eastern desert, Egypt. *World J Eng* 12:563–576
 49. Abd El-Wahed MA (2010) The role of the Najd Fault System in the tectonic evolution of the Hammamat molasse sediments, Eastern Desert, Egypt. *Arab J Geosci* 3:1–26
 50. Fritz H, Abdelsalam M, Ali KA, Bingen B, Collins AS, Fowler AR, Ghebream W, Hauzenberger CA, Johnson PR, Kusky TM, Macey P, Muhongo S, Stern RG, Viola G (2013) Orogen styles in the East African Orogen: a review of the Neoproterozoic to Cambrian tectonic evolution. *J Afr Earth* 86:65–106
 51. Aeroservice (1984) Final operational report of airborne magnetic/radiation survey in the Eastern Desert, Egypt for the Egyptian General Petroleum Corporation. Aero-Service Division, Houston, Western Geophysical Co., Texas, p 250
 52. Baranov V (1957) A new method for interpretation of aeromagnetic maps: Pseudo-gravimetric anomalies. *Geophysics* 22:359–383
 53. Pal SK, Vaish J, Kumar S, Bharti AK (2016) Coalfire mapping of East Basuria Colliery, Jharia coal field using Vertical Derivative Technique of Magnetic data. *J Earth Syst Sci* 125:165–178
 54. Pal SK, Narayan S, Majumdar TJ, Kumar U (2016) Structural mapping over the 850E ridge and surroundings using EIGEN6C4 High Resolution Global Combined Gravity Field Model: an integrated approach. *Mar Geophys Res* 37:159–184
 55. Pal SK, Vaish J, Kumar S, Priyam P, Bharti AK, Kumar R (2017) Downward continuation and Tilt Derivative of magnetic data for delineation of concealed coal fire in East Basuria Colliery, Jharia coal field, India. *J Earth Syst Sci* 126:53
 56. Ganguli SS, Singh S, Das N, Maurya D, Pal SK, Rama Rao JV (2019) Gravity and magnetic survey in south western part of Cuddapah Basin, India and its implication for shallow crustal architecture and mineralization. *J Geol Soc India* 93:419–430
 57. Ganguli SS, Pal SK, Rama Rao JV, Sunder Raj B (2020) Gravity-magnetic appraisal at the interface of Cuddapah Basin and Nellore Schist Belt (NSB) for shallow crustal architecture and tectonic settings. *J Earth Syst Sci* 129:92
 58. Spector A, Grant FS (1970) Statistical models for interpreting aeromagnetic data. *Geophysics* 35:293–302
 59. Mousa A, Mickus K, Al-Rahim A (2017) The thickness of cover sequences in the Western Desert of Iraq from a power spectrum analysis of gravity and magnetic data. *J Asian Earth Sci* 138:230–245
 60. Ganguli SS, Pal SK, Singh SL, Rama Rao JV, Balakrishna B (2020) Insights into crustal architecture and tectonics across Palghat Cauvery Shear Zone, India from combined analysis of gravity and magnetic data. *Geol J* 55:1–19
 61. Ganguli SS, Pal SK, Sundaralingam K, Kumar P (2021) Insights into the crustal architecture from combined analysis of gravity and magnetic data across Salem Attur Shear Zone (SASZ), Southern Granulite Terrane (SGT), India: An evidence of accretional tectonics. Episodes <https://doi.org/10.18814/epiiugs/2020/020095>
 62. Roest WR, Verhoef J, Pilkington M (1992) Magnetic interpretation using the 3-D analytic signal. *Geophysics* 57:116–125

63. Geosoft (2007) Geosoft mapping and application system. Inc, Suit 500, Richmond St. West Toronto, ON Canada N5S1V6
64. GETECH (2007) Advanced Processing and Interpretation of Gravity and Magnetic Data. GETECH Plc., UK, p 27
65. Miller HG, Singh V (1994) Potential field tilt-a new concept for location of potential field sources. *J Appl Geophys* 32:213–217
66. Pal SK, Majumdar TJ (2015) Geological appraisal over the Singhbhum-Orissa Craton, India using GOCE, EIGEN6-C2 and in-situ gravity data. *Int J Appl Earth Obs Geoinf* 35:96–119
67. Thurston JB, Smith RS (1997) Automatic conversion of magnetic data to depth, dip, and susceptibility contrast using the SPI(TM) method. *Geophysics* 62:807–813

Publisher's Note Springer Nature remains neutral with regard to jurisdictional claims in published maps and institutional affiliations.